Applied Physics Letters ARTICLE scitation.org/journal/apl

Band alignment and defects influence the electron–phonon heat transport mechanisms across metal interfaces

Cite as: Appl. Phys. Lett. **118**, 163503 (2021); doi: 10.1063/5.0046566
Submitted: 4 February 2021 · Accepted: 3 April 2021 ·
Published Online: 20 April 2021

David H. Olson,[1] Maria G. Sales,[2] John A. Tomko,[1] Teng-Fei Lu,[3] Oleg V. Prezhdo,[4] Stephen J. McDonnell,[2] and Patrick E. Hopkins[1,2,5,a)]

AFFILIATIONS

[1]Department of Mechanical and Aerospace Engineering, University of Virginia, Charlottesville, Virginia 22904, USA
[2]Department of Materials Science and Engineering, University of Virginia, Charlottesville, Virginia 22904, USA
[3]School of Materials Science and Engineering, Dalian Jiaotong University, Dalian 116028, Liaoning Province, China
[4]Department of Chemistry, University of Southern California, Los Angeles, California 90089, USA
[5]Department of Physics, University of Virginia, Charlottesville, Virginia 22904, USA

[a)]Author to whom correspondence should be addressed: phopkins@virginia.edu

ABSTRACT

We report on the experimental determination of electron–electron conductance at Au/TiO_x interfacial regions and electron–phonon coupling of thin TiO_x layers for $x = 0$–2.62. Our study demonstrates that the electronic energy transport mechanisms at metal/metal oxide interfaces are enhanced through metallic defects that lead to electronic band alignment between the metal and metal oxide (in our case, Au and TiO_x). Electronic heat transport processes are interrogated via a pump/probe technique, utilizing sub-picosecond laser pulses to monitor the ultrafast thermoreflectance responses of Au/TiO_x systems, which were analyzed using a two-temperature model to extract electron–electron conductances at Au/TiO_x interfaces and the electron–phonon coupling in TiO_x layers. We find that TiO_x stoichiometries near TiO_2 have ultrahigh electron–phonon coupling factors similar to that of pure Ti and that electronic energy transmission from Au to TiO_x layers is comparable to that of Au to Ti due to the presence of Ti^0 defects. For $x = 2.62$ in TiO_x, electron–phonon coupling is reduced by more than a factor of 5. Our experimental data are corroborated by real-time time-dependent density functional theory calculations, which show that excited electrons in Au do not participate in the TiO_x phonon relaxation process, resulting in lower electron–electron energy transmission from Au and electron–phonon coupling due to the difference in the Fermi energy of Au relative to the conduction band minimum of TiO_x when $x > 2$.

The interaction between excited electrons and phonons is fundamental to the functionality of a range of devices and technologies, such as photovoltaics,[1–4] catalysis,[5,6] and optoelectronics.[7–10] Photovoltaics, in particular, rely on the lack of recombination of charge carriers prior to reaching electrodes, and thus a low electron/hole–phonon coupling rate is necessary for optimizing efficiency. As a result of this condition, TiO_2 is ubiquitously used in the photovoltaic industry due to its low recombination rate, wide-bandgap, and higher conduction band (CB) edge energy.[11,12] In perovskite solar cells, TiO_2 layers have been implemented adjacent to the photoactive perovskite to facilitate fast electron transport to the transparent conducting oxide and maximize efficiency by reducing electron–phonon coupling.[13]

Unsurprisingly, defects present in TiO_2 layers have been shown to inhibit the maximum attainable quantum efficiency, η, of solar cells. In one study, η was reduced by more than a factor of two in TiO_2 films containing oxygen vacancies.[14] In another, oxygen vacancies were correlated with second order scattering modes, alongside the presence of Ti^{4+}/Ti^{3+} mixed states.[15] Both of these factors decreased η by a factor of ∼2–4 as a result of an increase in the charge recombination rate as a result of an increased number of coupling pathways.[16] Further, Radecka *et al.*[17] have examined stoichiometry influences in oxygen deficient TiO_{2-x} films, where an increase in oxygen deficiency was correlated with a reduction in charge carrier mobility. Sharma *et al.*[18] have also shown that nonstoichiometry reduces η by a factor of two. Clearly, the defect concentration is integral in the performance of photovoltaic devices, impacting electron–phonon coupling, and must be accounted for during the fabrication process.

In this paper, we study the effects of oxygen stoichiometry in TiO_x layers on electron–phonon coupling and resulting energy

transport mechanisms, schematically illustrated in Fig. 1(a). This is accomplished by implementing ultrafast pump–probe spectroscopy to examine the nonequilibrium carrier dynamics of Au/TiO_x/Al_2O_3 systems and quantifying the electron–phonon coupling factor, g, of thin TiO_x layers whose stoichiometry and thickness range from $x = 0$–2.62 to $d = 0$–4 nm, respectively. Additionally, we determine the efficiency of electron thermal transport across the Au/TiO_x interfacial region, quantified by the electron–electron thermal boundary conductance.[19–21] We find that both of these transport mechanisms are heavily influenced by the stoichiometry of the TiO_x layer, where residual metallic Ti^0 allows for more efficient electron–phonon coupling in the adhesion layer and electron energy transport at the Au/TiO_x interface as a result of the better band alignment between the Au and TiO_x, as quantified by real-time time-dependent density functional theory.

Energy transport from a photonically excited electronic system of a metal contact to the phononic system of a dielectric substrate through an adhesion layer consists of numerous energy transport mechanisms within and between layers at ultrafast (<1000 ps) timescales. First, energy is deposited into the electronic system of the top metal contact via photon absorption. Electrons in this layer will traverse through the layer and scatter with a phonon at an average length scale of the mean free path. At the Au/TiO_x interface, the efficiency of electron interfacial energy transport can be described by the electron diffuse mismatch model (EDMM).[19] In short, the electron–electron interfacial conductance, G_{ee}, is proportional to the average electron temperature on either side of the interface, $T_{e,avg}$, via the ratio of the electronic densities of states and Fermi velocities, Γ. As electrons traverse the Au/TiO_x interface, they couple to the lattice in the TiO_x layer, increasing its temperature. This creates a temperature disparity between the top Au contact and underlying dielectric substrate in the electronic and lattice systems. Ultimately, this results in an indirect heating of the Au lattice temperature as a result of the mismatch in electron–phonon coupling with the TiO_x layer which can be probed using ultrafast pump/probe spectroscopy.

To explore the effects of oxygen stoichiometry and thickness on electron–phonon coupling in TiO_x, as well as electron energy transfer at the Au/TiO_x interface, we monitor the sub-picosecond to nanosecond excitation and relaxation processes of Au/TiO_x samples with time-domain thermoreflectance. The specific samples and characterization of these samples are detailed in our prior work.[22] Briefly, 4 nm layers of TiO_x were deposited in a high vacuum (HV) environment ($\sim 1 \times 10^{-6}$ Torr) at 0.1, 0.5, and 1.0 Å/s on a set of Al_2O_3 substrates. Due to the HV conditions during evaporation, the deposition resulted in TiO_x with varying x based on the Ti deposition rate when assuming a consistent codeposition of oxidizing species across all specimens during the deposition procedure.[22] This TiO_x adhesion layer was capped with ~3 nm Au, and one of the substrates was removed from the chamber for characterization via x-ray photoelectron spectroscopy (XPS). The other was pumped down once again and capped with an additional ~50 nm Au to facilitate thermal measurements via time-domain thermoreflectance.[23,24] For comparative purposes, we fabricate systems without an adhesion layer (i.e., just 50 nm Au on Al_2O_3), as well as one with a 1 nm Ti adhesion layer deposited at ~0.1 Å/s in ultrahigh vacuum (UHV) capped with 50 nm Au. The thickness of the Au layer for all these specimens, ~50 nm, is ideal in maximizing sensitivity to measurements of the electron–phonon coupling factor, g, and the electron–electron thermal boundary conductance, Γ, while minimizing additional optical thermoreflectance responses from the underlying TiO_x layer that can obfuscate analysis (cf., supplementary material Sec. S2).

XPS spectra of the specimens with a TiO_x adhesion layer are shown in Fig. 1 for the (b) O 1s and (c) Ti 2p spectra of the TiO_x adhesion layers. Spectral deconvolution was performed on both spectra in order to determine (1) the fraction of oxygen that reacted with Ti to form TiO_x during the deposition process and (2) the fraction of unreacted Ti present in the layer, Ti^0. At 0.1 Å/s, approximately ~50% of the oxygen present in the adhesion layer comes directly from TiO_x, with the other ~50% coming from hydrocarbon and hydroxide species. On the other hand, oxygen from TiO_x comprised ~75% of the oxygen present in specimens deposited at 0.5 and 1.0 Å/s. At 0.1 Å/s in UHV, no oxygen originating from Ti–O bonds was found—the signature at ~532 eV is of the Al_2O_3 substrate and is detectable due to the

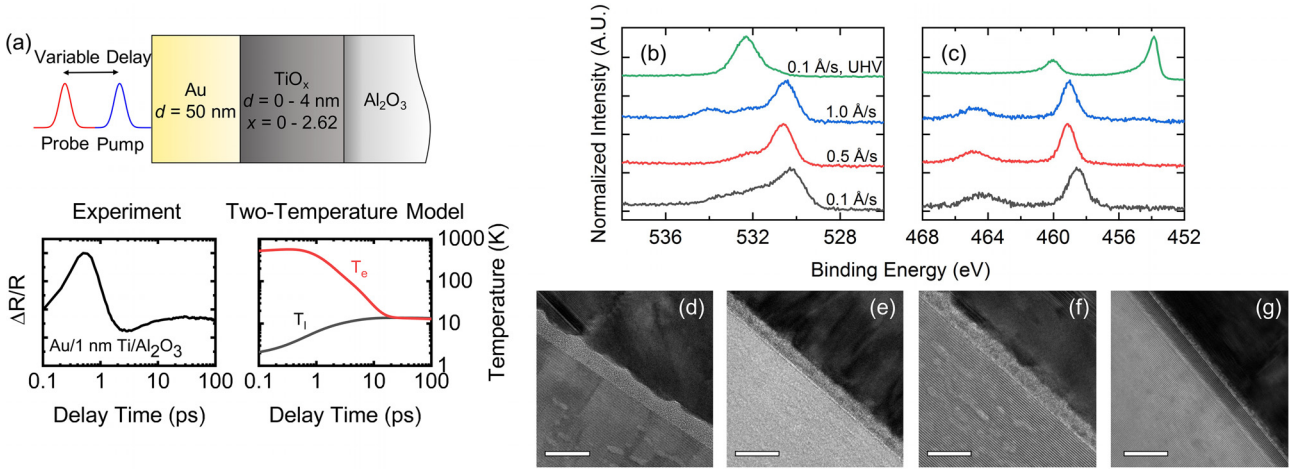

FIG. 1. (a) Optical pump/probe experiment for determining energy transfer mechanisms in Au/TiO_x structures. T_e and T_l are the surface temperature excursions of the electronic and lattice systems, respectively, in Au/1 nm Ti/Al_2O_3 as determined via the two-temperature model. (b) O 1s and (c) Ti 2p spectra of TiO_x adhesion layers deposited in HV and UHV. TEM micrographs of adhesion layers deposited at (d) 0.1, (e) 0.5, and (f) 1.0 Å/s in HV and at (g) 0.1 Å/s in UHV. In (d)–(g), the scale bar is 5 nm.

thinness of the layer (1 nm). From the Ti 2*p* spectra, Fig. 1(c), spectral deconvolution indicates that the composition of Ti present at 0.1 and 0.5 Å/s is entirely of reacted Ti, Ti^{4+}. At 1.0 Å/s, however, the small signature at ∼455 eV indicates that approximately 4% of the layer comprised of unreacted Ti, Ti^0. In all, the O:Ti ratios of the TiO_x layers deposited in HV, when accounting for only O–Ti features, were 2.62, 2.06, and 1.90 for specimens deposited at 0.1, 0.5, and 1.0 Å/s, respectively, while the specimen deposited in UHV appears purely metallic.

Shown in Figs. 1(d)–1(g) are TEM micrographs of each specimen at the Au/TiO_x/Al_2O_3 interfacial regions. All samples deposited in HV show a consistent thickness of 3–4 nm and no signs of island formation. For the specimen deposited in UHV, Fig. 1(g), the thickness of the adhesion layer is consistent with that determined via XPS, ∼1 nm. In the specimens deposited in HV, there is a noticeable difference in the structure between the samples deposited at 0.1 Å/s and those deposited at 0.5 and 1.0 Å/s. At 0.1 Å/s, the adhesion layer is completely amorphous, while at 0.5 and 1.0 Å/s, the interfacial layers show pockets of crystallinity. We are unsure of the exact reasons for the amorphous nature of the adhesion layer deposited at 0.1 Å/s in HV. Considering that the layer deposited at approximately the same deposition rate in UHV was crystalline, we hypothesize that the codeposition of oxidizing species in HV played some role in the crystallization kinetics during the deposition of the layer.

We measure the ultrafast electron thermal transport mechanisms of the Au/TiO_x samples with time-domain thermoreflectance (TDTR), an optical pump/probe technique. See the supplementary material Sec. S1 for additional details regarding TDTR. The acquired thermal decay is typically compared to the heat diffusion equation; however, at short, ultrafast timescales, where the dynamic interplay between electrons and phonons is most prevalent, the two-temperature model[33] (TTM) is implemented. Governed by the coupled partial differential equations,

$$\begin{aligned} C_e\frac{\partial T_e}{\partial t} &= \nabla\cdot(\kappa_e\nabla T_e) - g(T_e - T_l) + S(x,t) \\ C_l\frac{\partial T_l}{\partial t} &= \nabla\cdot(\kappa_l\nabla T_l) + g(T_e - T_l), \end{aligned} \tag{1}$$

the TTM considers both electrons and phonons as separate carriers of heat. In these equations, C_e and C_l are the electronic and lattice heat capacities, respectively, T_e and T_l are the electronic and lattice temperatures, κ_e and κ_l are the electronic and lattice thermal conductivities, and g is the electron–phonon coupling factor. In the Au capping and TiO_x adhesion layers, the electronic heat capacities are defined such that $C_e = \gamma T_e$, where γ is the electron heat capacity coefficient.[26,34] $S(x, t)$ is the source term, which deposits energy into the electronic system, defined as

$$S(x,t) = -0.94\frac{1-R}{t_p}J\cdot\exp\left[-2.77\left(\frac{t}{t_p}\right)^2\right]\frac{dI}{dx}. \tag{2}$$

In this equation, J is the fluence, R is the surface reflectivity, t_p is the duration of the pump pulse, and x and t are the space and time variables, respectively. $\frac{dI}{dx}$ is the spatial derivative of the light intensity distribution in the sample, calculated using a transfer matrix method with the indices of refraction, n, at our pump wavelength of 400 nm.

Equations (1) and (2) are solved numerically using the Crank–Nicolson method.[35] Unless otherwise stated, all inputs into the model can be found in Table I. For the Au/Al_2O_3 system, we fit for g of the Au film and the phonon conductance at the Au/Al_2O_3 interface. In systems with a TiO_x adhesion layer, we fit for g of the adhesion layer, Γ at the Au/TiO_x interface, as well as the phonon conductance at the TiO_x/Al_2O_3 interface. See the supplementary material Sec. S3 for additional details regarding the modeling and fitting procedure.

TABLE I. Parameters utilized in TTM modeling and fitting. For each layer, d is the thickness, C_l is the lattice heat capacity, γ is the electronic heat capacity coefficient, κ_e and κ_l are the electronic and lattice thermal conductivities, respectively, g is the electron–phonon coupling factor, n is the complex refractive index, and dn/dT is the temperature derivative of the complex refractive index. Fitting parameters are designated by **F** in Au, Au/TiO_x, and Au/Ti systems. In Au/TiO_x and Au/Ti systems, we also fit for Γ, the proportionality constant for the electron–electron thermal conductance.

	Au	TiO_x	Ti	Al_2O_3
d (nm)	50[a]	4	1	
C_l (MJ m^{-3} K^{-1})	2.49[b]	2.83[b]	2.36[b]	3.06[b]
γ (J m^{-3} K^{-2})	63[c]	329[c]	329[c]	
κ_e (W m^{-1} K^{-1})	276[d]	1[e]	10[b]	
κ_l (W m^{-1} K^{-1})	3[f]	1	2[b]	35
g (10^{16} W m^{-3} K^{-1})	**F** (Au)	**F** (Au/TiO_x)	**F** (Au/Ti)	
n (400 nm)	1.47 + i1.95[g]	2.37[h]	2.09 + i2.96[g]	1.79[i]
n (800 nm)	0.15 + i4.91[g]	2.10[h]	3.14 + i4.01[g]	1.76[i]
$dn/dT\times 10^4$ (800 nm)	2.1[j]	2.1[j]	2.1[j]	

[a]Measured using X-ray reflectivity.
[b]Reference 25.
[c]Reference 26.
[d]Determined using four-point probe and the Wiedemann–Franz law.
[e]Reference 27.
[f]Reference 28.
[g]Reference 29.
[h]Reference 30.
[i]Reference 31.
[j]Reference 32.

Figure 2 shows the acquired ultrafast reflectivity and best fits for the Au/TiO_x systems in the range of $x = 0$–2.62, alongside Au for reference. The response of $TiO_{2.06}$ was not included because of its similarity to $TiO_{1.90}$. At short time scales (<4 ps), a sharp increase in the reflectivity followed by its decay is observed across all specimens due to the dynamic electron temperature following optical excitation. At longer time scales (>4 ps), the response depends on the composition of the adhesion layer. For the system lacking an adhesion layer, the reflectivity is approximately constant and decays slightly. On the other hand, systems with an adhesion layer exhibit a rise in reflectivity compared to that at ∼3 ps. Both the rate at which this rise occurs and its final magnitude depend on the stoichiometry of the underlying adhesion layer and are characteristic of electron energy transport and the mismatch of electron–phonon coupling factors in metal/metal[36–38] and metal/semiconductor[39] systems.

The extracted g and Γ for all systems are presented in Figs. 3(a) and 3(b), respectively. For systems with a TiO_x adhesion layer, we cannot distinguish between the intrinsic transport characteristics of g and Γ and those due to the nanometer roughness at the Au/TiO_x interface. Our reported values, therefore, reflect both intrinsic transport mechanisms within the TiO_x and at the Au/TiO_x interfaces, as well as

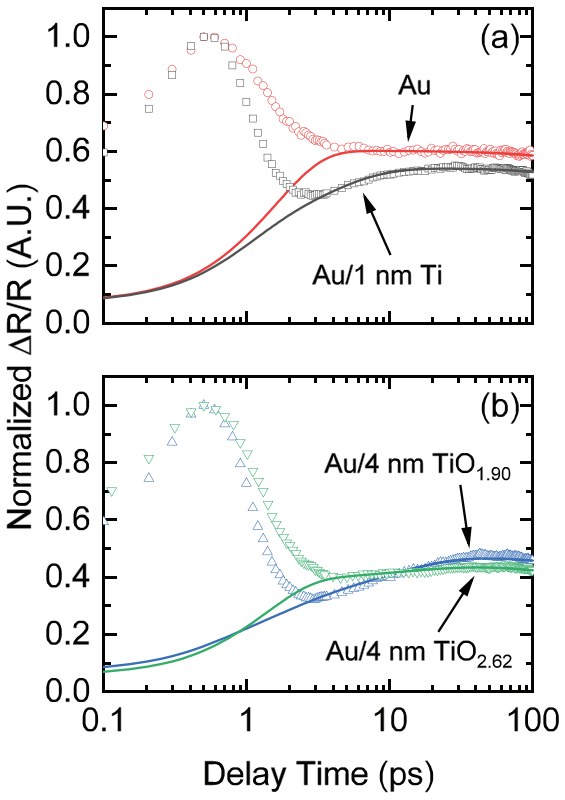

FIG. 2. Ultrafast data and TTM best fits (>3 ps) for (a) Au and Au/1 nm Ti and (b) Au/4 nm TiO_x systems.

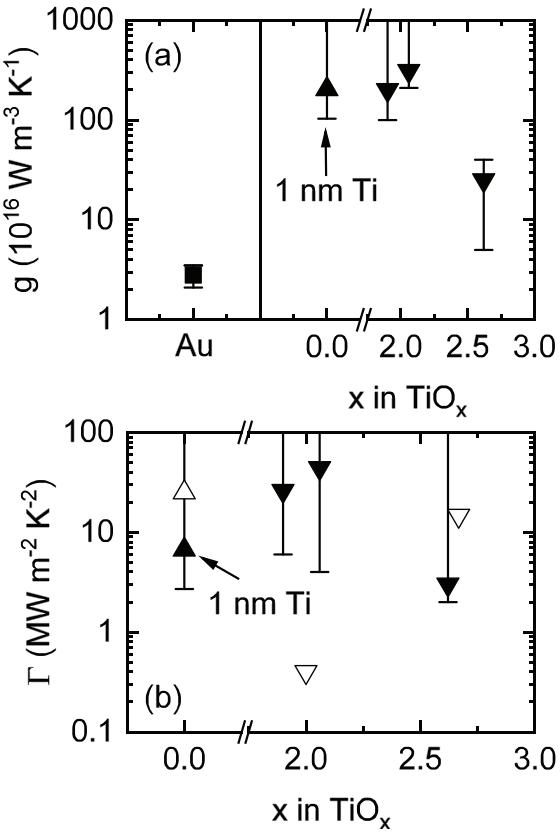

FIG. 3. Experimentally determined (a) electron–phonon coupling (g) of TiO_x wetting layers and (b) coefficient of electron–electron thermal conductance (Γ) at Au/TiO_x interfaces. Filled symbols are experimentally determined, while open symbols are predicted by the electronic diffuse mismatch model (EDMM) for stoichiometric Ti, TiO_2, and Ti_3O_8.

the contribution from any extrinsic effects as a result of the roughness at the Au/TiO_x interfacial region. We determine the electron–phonon coupling factor of Au to be $2.8 \pm 0.7 \times 10^{16}$ W m^{-3} K^{-1}, in reasonable agreement with previously reported values.[41–44] The predicted value for the electron–phonon coupling factor in Ti is $\sim 150 \times 10^{16}$ W m^{-3} K^{-1} at room temperature.[26] This large value, coupled with the small thickness, d, of the adhesion layer results in a large electron–phonon conductance in the Ti layer, gd. As a result, we set a lower limit on the electron–phonon coupling factor of Ti as values above 100×10^{16} W m^{-3} K^{-1} offer comparable fits to our data. We find g of the oxygenated adhesion layers with stoichiometries $TiO_{1.90}$ and $TiO_{2.06}$ to be similar to that of the 1 nm pure Ti layer, $>100 \times 10^{16}$ W m^{-3} K^{-1}. This high g in a highly defected TiO_x layer is likely due to the fact that residual, unreacted Ti is present in these films, allowing for a low resistance pathway from the Au to TiO_x adhesion layer. Indeed, we observe that ~4% of the Ti in $TiO_{1.90}$ layer consists of unreacted Ti^0. We note that while the presence of Ti^0 cannot be confirmed via XPS in the specimen with a stoichiometry of $TiO_{2.06}$, g for this layer is still comparable to that of pure Ti. This suggests that fractions of Ti less than the detectable limits of XPS (~0.5%–1%) are still able to significantly impact the transport processes in these systems. Once the oxygen concentration of the adhesion layer is greatly increased, reaching a stoichiometry of $TiO_{2.62}$, no residual Ti^0 can be confirmed, and this low resistance pathway is not present. We find that g for the $TiO_{2.62}$ layer is ~25×10^{16} W m^{-3} K^{-1}, suggesting that coupling still occurs in the $TiO_{2.62}$ layer at a rate that exceeds that of the Au film.

Figure 3(b) shows the results for the electronic thermal conductance coefficient, Γ. As with g in the 1 nm Ti adhesion layer, the incredibly high electron–electron conductance at the Au/Ti interface makes g and Γ difficult to quantify. Indeed, the electronic diffuse-mismatch model predicts Γ to be 25 MW m^{-2} K^{-2} or an equivalent conductance of nearly 7.5 GW m^{-2} K^{-1} at room temperature. We can thus only place a lower bound on Γ as equivalent fits in our model are found for when $\Gamma > 2$ MW m^{-2} K^{-2}. EDMM calculations of Γ, shown as open symbols in Fig. 3(b), using the electron density of states (DOS) from Fig. 4, exemplify the importance of stoichiometry in these models. In particular, due to the presence of Ti^0 in our TiO_x films, our measured Γ exceeds the theoretical value for Au/TiO_2 by an order of magnitude. Additionally, the measured lower bound for Γ in $TiO_{2.62}$, which has a stoichiometry that is close to Ti_3O_8, is in reasonable agreement with the EDMM predicted value for Au/Ti_3O_8.

To better understand the reasons for our measured g and Γ, we focus on examining stoichiometric effects in Au/Ti_xO_y on electron–phonon relaxation times using real-time time-dependent density functional theory (TDDFT),[40] the simulation details of which

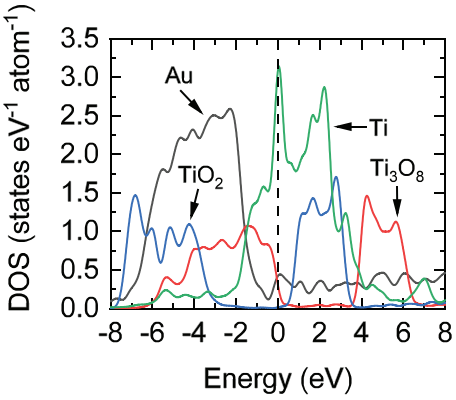

FIG. 4. Electron density of states (DOS) of Au, Ti, TiO_2, and Ti_3O_8 from Lu *et al.*[40] Reproduced with permission from Lu *et al.*, J. Phys. Chem. Lett. **11**, 4 (2020). Copyright 2020 American Chemical Society.[40]

can be found in supplementary material Sec. S4. In Fig. 5, we plot the (a) picosecond pump/probe dynamics of our Au/TiO_x systems alongside the (b) electron energy decay of Au/Ti_xO_y calculated using TDDFT in Ref. 40. Because the short-time response of our acquired data is indicative of the electron temperatures of Au and TiO_x in our specimens, we normalize the data such that the signal decays to 0 at 3 ps for comparative purposes only. This approximately reflects the time at which the energy of the excited electrons has decayed to 0 eV, allowing us to make direct comparisons to the TDDFT predictions. We also adjust the 0 time delay to the maximum of the acquired signal.

We find that the measured relaxation times of our Au/TiO_x systems are in qualitative agreement with those derived from TDDFT. In Au and Au/$TiO_{2.62}$ systems, we determine relaxation times of ~650 fs. For Au/TiO_x systems for $x = 0$, 1.90, and 2.06, the relaxation time is faster, ~420 fs. Our measured relaxation times reflect electron–electron as well as electron–phonon interactions. Lu *et al.*[40] determined relaxation times of 2.75, 2.85, 1.99, and 0.75 ps for Au, Au/Ti_3O_8, Au/TiO_2, and Au/Ti systems, respectively. We cannot make direct comparisons to Ref. 40 due to the fact that they do not account for

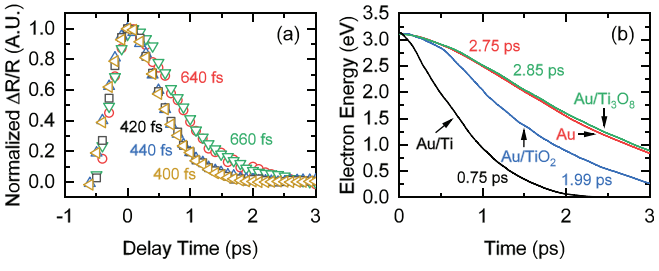

FIG. 5. (a) Normalized ultrafast response of Au films with a TiO_x wetting layer. Red circles are for the Au system, green down-facing triangles are for the Au/$TiO_{2.62}$ system, gold left-facing triangles are for the Au/$TiO_{2.06}$ system, blue up-facing triangles are for the Au/$TiO_{1.90}$ system, and black squares are for the Au/1 nm Ti system. (b) Electron relaxation dynamics from Lu *et al.*[40] for Au/Ti_xO_y systems. Reproduced with permission from Lu *et al.*, J. Phys. Chem. Lett. **11**, 4 (2020). Copyright 2020 American Chemical Society.[40]

electron–electron interactions and the simulation is not able to capture all electronic and phononic states due to its size. However, we find that our derived relaxation times trend well with those of Lu *et al.*[40] when considering the minute differences in stoichiometry.

The reason for the decreased relaxation time in Au/TiO_x systems for $x = 0$, 1.90, and 2.06 is influenced by a variety of factors, including (1) the presence of Ti^0, (2) the excited electron energy relative to the Fermi energy, and (3) the relative position of the Fermi energy in Au to the conduction and valence bands (VBs) of TiO_x.

Primarily, Ti^0 atoms present in $TiO_{1.90}$ and $TiO_{2.06}$ accelerate the relaxation time due to the higher g of Ti. As the fraction of Ti^0 in these layers is small as confirmed via XPS, and the composition is nominally TiO_2, lighter Ti and O atoms in TiO_2 move faster to help increase electron–phonon coupling compared to Au. Indeed, inspection of the nonadiabatic electron–phonon coupling matrix element, $i\hbar\langle\Phi_j|\nabla_R|\Phi_k\rangle \cdot d\boldsymbol{R}/dt$, which describes the transition between electronic states j and k by coupling to phonons, is proportional to the phonon velocity, $d\boldsymbol{R}/dt$.[45]

Additionally, the alignment of the TiO_x energy levels with respect to the Au Fermi energy influences charge-phonon relaxation, see Fig. 4. For an accelerated relaxation process to occur, the energy of excited electrons in the Au must fall outside of the TiO_x bandgap so that they may interact with those in the adhesion layer. As the incident photon energy (3.1 eV) generates the same number of electrons and holes, an equivalent number of conductance and valence band orbitals will be involved in the photoexcitation process. Since the hole DOS is larger than the electron DOS in Au, the generation of a particular number of hole states requires a smaller energy range compared to the same number of electron states. Thus, as a result of this asymmetry in DOS, the photoexcitation process covers a broader range of electron state energies, and electrons therefore accommodate the majority of the incident photon energy. Excited electrons in the Au will, therefore, be above the bandgap of TiO_2, increasing coupling.

Further, the Au Fermi energy is within ~1 eV of the conduction band (CB) minimum of TiO_2, resulting in a resonance of the TiO_2 CB states and Au electrons near the Fermi energy and increasing electron–phonon relaxation. The Au Fermi energy is also within ~0.5 eV of the valence band (VB) maximum for Ti_3O_8, whose stoichiometry is close to $TiO_{2.62}$. At this stoichiometry, electrons excited to 3.1 eV above the Au Fermi energy fall within the bandgap of the adhesion layer, and thus electron–phonon coupling is subdued due to the fact electrons in the $TiO_{2.62}$ layer cannot participate in the process resulting in a comparable relaxation time to the system lacking an adhesion layer.

In summary, we performed ultrafast pump/probe measurements for the determination of the electron–phonon coupling factors of thin TiO_x layers and the associated electron–electron conductance across the Au/TiO_x interface. Our results are indicative of the fact that even a small fraction of unreacted Ti in TiO_x adhesion layers has a significant impact on the associated energy transfer mechanisms across Au/TiO_x interfacial regions. TiO_x layers with stoichiometries close to TiO_2, when unreacted Ti is still present, offer comparable electron–phonon coupling factors and electron–electron thermal boundary conductances to that of pure Ti. The data are in agreement with real-time TDDFT calculations, and the results provide fundamental insight into applications requiring the use of metal oxide nanoscale films and interfaces in systems where charge relaxation plays a significant role in optimizing efficiencies.

See the supplementary material for a description of TDTR, experimental insight into the electron–phonon relaxation length scales, parameters used in two-temperature modeling, and a description of real-time time-dependent density functional theory calculations.

We appreciate support from the Office of Naval Research, Grant No. N00014-18-1-2429 and the Army Research Office, Grant No. W911NF-16-1-0406. D. H. Olson is grateful for funding from the National Defense Science and Engineering Graduate (NDSEG) Fellowship.

DATA AVAILABILITY

The data that support the findings of this study are available from the corresponding author upon reasonable request.

REFERENCES

[1]M. B. Johnston and L. M. Herz, "Hybrid perovskites for photovoltaics: Charge-carrier recombination, diffusion, and radiative efficiencies," Acc. Chem. Res. **49**(1), 146–154 (2016).
[2]J. Krüger, R. Plass, L. Cevey, M. Piccirelli, M. Grätzel, and U. Bach, "High efficiency solid-state photovoltaic device due to inhibition of interface charge recombination," Appl. Phys. Lett. **79**(13), 2085–2087 (2001).
[3]A. Pivrikas, N. S. Sariciftci, G. Juska, and R. Osterbacka, "A review of charge transport and recombination in polymer/fullerene organic solar cells," Prog. Photovoltaics: Res. Appl. **15**, 677–696 (2007).
[4]Z. Nie, X. Gao, Y. Ren, S. Xia, Y. Wang, Y. Shi, J. Zhao, and Y. Wang, "Harnessing hot phonon bottleneck in metal halide perovskite nanocrystals via interfacial electron-phonon coupling," Nano Lett. **20**(6), 4610–4617 (2020).
[5]R. Qian, H. Zong, J. Schneider, G. Zhou, T. Zhao, Y. Li, J. Yang, D. W. Bahnemann, and J. H. Pan, "Charge carrier trapping, recombination and transfer during TiO_2 photocatalysis: An overview," Catal. Today **335**, 78–90 (2019).
[6]L. Hammarström, "Accumulative charge separation for solar fuels production: Coupling light-induced single electron transfer to multielectron catalysis," Acc. Chem. Res. **48**(3), 840–850 (2015).
[7]U. Albrecht and H. Bässler, "Efficiency of charge recombination in organic light emitting diodes," Chem. Phys. **199**(2-3), 207–214 (1995).
[8]J. Kalinowski, M. Cocchi, P. D. Marco, W. Stampor, G. Giro, and V. Fattori, "Impact of high electric fields on the charge recombination process in organic light-emitting diodes," J. Phys. D **33**(19), 2379–2387 (2000).
[9]W. G. Scheibenzuber, U. T. Schwarz, L. Sulmoni, J. Dorsaz, J. F. Carlin, and N. Grandjean, "Recombination coefficients of GaN-based laser diodes," J. Appl. Phys. **109**(9), 093106 (2011).
[10]L. A. Coldren, S. W. Corzine, and M. L. Masanovic, *Diode Lasers and Photonic Integrated Circuits*, 2nd ed. (John Wiley & Sons, Ltd., 2011).
[11]S. Na-Phattalung, M. F. Smith, K. Kim, M. H. Du, S. H. Wei, S. B. Zhang, and S. Limpijumnong, "First-principles study of native defects in anatase TiO_2," Phys. Rev. B **73**(12), 125205 (2006).
[12]Y. Bai, I. Mora-Seró, F. De Angelis, J. Bisquert, and P. Wang, "Titanium dioxide nanomaterials for photovoltaic applications," Chem. Rev. **114**(19), 10095–10130 (2014).
[13]R. Kentsch, M. Scholz, J. Horn, D. Schlettwein, K. Oum, and T. Lenzer, "Exciton dynamics and electron-phonon coupling affect the photovoltaic performance of the $Cs_2AgBiBr_6$ double perovskite," J. Phys. Chem. C **122**(45), 25940–25947 (2018).
[14]T. K. Das, P. Ilaiyaraja, and C. Sudakar, "Template assisted nanoporous TiO_2 nanoparticles: The effect of oxygen vacancy defects on photovoltaic performance of DSSC and QDSSC," Sol. Energy **159**, 920–929 (2018).
[15]T. K. Das, P. Ilaiyaraja, P. S. Mocherla, G. M. Bhalerao, and C. Sudakar, "Influence of surface disorder, oxygen defects and bandgap in TiO_2 nanostructures on the photovoltaic properties of dye sensitized solar cells," Sol. Energy Mater. Sol. Cells **144**, 194–209 (2016).
[16]X. Ma, Z. Cheng, M. Tian, X. Liu, X. Cui, Y. Huang, S. Tan, J. Yang, and B. Wang, "Formation of plasmonic polarons in highly electron-doped anatase TiO_2," Nano Lett. **21**, 430–436 (2021).
[17]M. Radecka, A. Brudnik, K. Kulinowski, A. Kot, J. Leszczyński, J. Kanak, and K. Zakrzewska, "Titanium dioxide thin films with controlled stoichiometry for photoelectrochemical systems," J. Electron. Mater. **48**(9), 5481–5490 (2019).
[18]V. Sharma, T. K. Das, P. Ilaiyaraja, and C. Sudakar, "Oxygen non-stoichiometry in TiO_2 and ZnO nano rods: Effect on the photovoltaic properties of dye and Sb_2S_3 sensitized solar cells," Sol. Energy **191**, 400–409 (2019).
[19]B. C. Gundrum, D. G. Cahill, and R. S. Averback, "Thermal conductance of metal-metal interfaces," Phys. Rev. B **72**(24), 245426 (2005).
[20]R. Cheaito, "The role of size effects on the thermal conductivity of thin film alloys and superlattices approval sheet," Ph.D. dissertation (University of Virgina, 2015).
[21]R. B. Wilson and D. G. Cahill, "Experimental validation of the interfacial form of the Wiedemann-Franz law," Phys. Rev. Lett. **108**(25), 255901 (2012).
[22]D. H. Olson, K. M. Freedy, S. J. McDonnell, and P. E. Hopkins, "The influence of titanium adhesion layer oxygen stoichiometry on thermal boundary conductance at gold contacts," Appl. Phys. Lett. **112**, 171602 (2018).
[23]C. A. Paddock and G. L. Eesley, "Transient thermoreflectance from thin metal films," J. Appl. Phys. **60**, 285–290 (1986).
[24]G. Tas and H. J. Maris, "Electron diffusion in metals studied by picosecond ultrasonics," Phys. Rev. B **49**, 15046 (1994).
[25]D. R. Lide, *CRC Handbook of Chemistry and Physics* (CRC Press LLC, Boca Raton, 2005).
[26]Z. Lin, L. V. Zhigilei, and V. Celli, "Electron-phonon coupling and electron heat capacity of metals under conditions of strong electron-phonon non-equilibrium," Phys. Rev. B **77**, 075133 (2008).
[27]E. A. Scott, J. T. Gaskins, S. W. King, and P. E. Hopkins, "Thermal conductivity and thermal boundary resistance of atomic layer deposited high-k dielectric aluminum oxide, hafnium oxide, and titanium oxide thin films on silicon," APL Mater. **6**(5), 058302 (2018).
[28]P. Klemens, "The lattice component of the thermal conductivity of metals and alloys," Aust. J. Phys. **7**(1), 57 (1954).
[29]P. B. Johnson and R. W. Christy, "Optical constant of the noble metals," Phys. Rev. B **6**(12), 4370–4379 (1972).
[30]S. Sarkar, V. Gupta, M. Kumar, J. Schubert, P. T. Probst, J. Joseph, and T. A. König, "Hybridized guided-mode resonances via colloidal plasmonic self-assembled grating," ACS Appl. Mater. Interfaces **11**(14), 13752–13760 (2019).
[31]I. H. Malitson and M. J. Dodge, "Refractive index and birefringence of synthetic sapphire," J. Opt. Soc. Am. **62**, 1405 (1972).
[32]R. B. Wilson, B. A. Apgar, L. W. Martin, and D. G. Cahill, "Thermoreflectance of metal transducers for optical pump-probe studies of thermal properties," Opt. Express **20**(27), 28829–22269 (2012).
[33]S. I. Anisimov, B. L. Kapeliovich, and T. L. Perel'man, "Electron emission from metal surfaces exposed to ultrashort laser pulses," Sov. Phys. JETP **39**(2), 375–377 (1974), available at http://jetp.ac.ru/cgi-bin/dn/e_039_02_0375.pdf.
[34]C. Kittel, *Introduction to Solid State* (John Wiley & Sons, 1966), Vol. 162.
[35]M. N. Ozisik, H. R. Orlande, M. J. Colaco, and R. M. Cotta, *Finite Difference Methods in Heat Transfer*, 2nd ed. (Taylor & Francis, Boca Raton, FL, 2017).
[36]G.-M. Choi, R. B. Wilson, and D. G. Cahill, "Indirect heating of Pt by short-pulse laser irradiation of Au in a nanoscale Pt/Au bilayer," Phys. Rev. B **89**(6), 064307 (2014).
[37]A. Giri, J. T. Gaskins, B. F. Donovan, C. Szwejkowski, R. J. Warzoha, M. A. Rodriguez, J. Ihlefeld, and P. E. Hopkins, "Mechanisms of nonequilibrium electron-phonon coupling and thermal conductance at interfaces," J. Appl. Phys. **117**, 105105 (2015).
[38]H. Jang, J. Kimling, and D. G. Cahill, "Nonequilibrium heat transport in Pt and Ru probed by an ultrathin Co thermometer," Phys. Rev. B **101**(6), 064304 (2020).
[39]J. A. Tomko, E. L. Runnerstrom, Y. S. Wang, W. Chu, J. R. Nolen, D. H. Olson, K. P. Kelley, A. Cleri, J. Nordlander, J. D. Caldwell, O. V. Prezhdo, J. P. Maria, and P. E. Hopkins, "Long-lived modulation of plasmonic absorption by ballistic thermal injection," Nat. Nanotechnol. **16**, 47 (2021).
[40]T. F. Lu, Y. S. Wang, J. A. Tomko, P. E. Hopkins, H. X. Zhang, and O. V. Prezhdo, "Control of charge carrier dynamics in plasmonic Au films by

TiO_x substrate stoichiometry," J. Phys. Chem. Lett. **11**(4), 1419–1427 (2020).
[41]J. L. Hostetler, A. N. Smith, D. M. Czajkowsky, and P. M. Norris, "Measurement of the electron-phonon coupling factor dependence on film thickness and grain size in Au, Cr, and Al," Appl. Opt. **38**(16), 3614 (1999).
[42]H. E. Elsayed-Ali, T. Juhasz, G. O. Smith, and W. E. Bron, "Femtosecond thermoreflectivity and thermotransmissivity of polycrystalline and single-crystalline gold films," Phys. Rev. B **43**, 4488–4491 (1991).
[43]R. H. M. Groeneveld, R. Sprik, and A. Lagendijk, "Femtosecond spectroscopy of electron-electron and electron-phonon energy relaxation in Ag and Au," Phys. Rev. B **51**, 11433–11445 (1995).
[44]J. Hohlfeld, S.-S. Wellershoff, J. Gudde, U. Conrad, V. Jahnke, and E. Matthias, "Electron and lattice dynamics following optical excitation of metals," Chem. Phys. **251**, 237–258 (2000).
[45]F. Giustino, "Electron-phonon interactions from first principles," Rev. Mod. Phys. **89**(1), 015003 (2017).